Additive Manufacturing 58 (2022) 103035

Contents lists available at ScienceDirect

Additive Manufacturing

journal homepage: www.elsevier.com/locate/addma

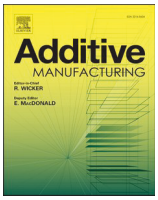

Analytical interpretation of microscale fiber deviation in designing for polymer melt electrohydrodynamic-based additive manufacturing

Kai Cao [a], Fucheng Zhang [a], Bijun Wang [b], Yuning Sun [b], Ahmadreza Zaeri [a], Ralf Zgeib [a], Mo Mansouri [b], Robert C. Chang [a,*]

[a] Department of Mechanical Engineering, Stevens Institute of Technology, USA
[b] School of Systems and Enterprises, Stevens Institute of Technology, USA

ARTICLE INFO

Keywords:
Melt electrohydrodynamic manufacturing
Curly fiber printing
Dynamic speed control
Toolpath-related fiber deviation

ABSTRACT

Aided by translational material collection, melt electrowriting is an additive electrohydrodynamic-based materials processing technique capable of fabricating fibrous 3D structured materials with customizable microscale architectures suitable for spatially defined tissue models. An inherent phenomenon of the melt electrowriting process is the characteristic jet lag, which results in spatial differences between the nozzle position (*np*) and the jet contact point (*cp*). Moreover, *cp* does not deterministically follow the *np* trajectory when the movement of *np* relative to the collector is directionally altered. Instead, fiber deviation related to the toolpath deteriorates the printing accuracy and is ubiquitous for curly fiber printing. In order to address this bottleneck, an analytical construct informed by fiber placement prediction and control is advanced. Specifically, by way of vector analysis and differential geometry, the position and speed relationships between *np* and *cp* are found to be governed by position- and speed-matching equations. Representations of these equations can be elaborated into the specific cases of straight and steady curly fiber printing, which are investigated and verified herein. Finally, the real-time identification of *cp* as well as dynamic control of translational stage speed are identified as critical steps towards reliable implementation of the toolpath design in curly fiber printing.

1. Introduction

As a melt electrohydrodynamic process aided by translational material collection, melt electrowriting (MEW) has shown promising applications in additive fabrication of microscale fibrous architectures for engineered tissue applications [1–3] due to its easy implementation [4,5], high resolution [6,7] and superior tunability [8–10]. The superior tunability of MEW-enabled 3D substrates is represented not only by the customizable homogeneous microarchitectures [11], but also by the heterogeneous microarchitectures with varying fiber diameters [12]. Moreover, in contrast to the traditional vertical stacking of layered fiber prints, an MEW-enabled structured material can be designed to exhibit structural variations in the layering direction by shifting the toolpath for each layer with recurrent offsets in the printing trajectory [13]. The quality of MEW-enabled print outcomes can be mainly evaluated by the uniformity of its constituent fibers and printing accuracy (i.e., how exactly the fibers are deposited along the prescribed toolpath). By systematically tuning the different process parameters, including the applied voltage U, the material temperature, and the translational stage speed v, it is feasible to customize the mean fiber diameter as well as overcome the 'fiber pulsing' phenomenon, thus enabling uniform outcomes in the fiber prints [14]. Maintenance of high printing accuracy, however, is a much more complex and nuanced manufacturing problem. The undesired fiber deviation from the prescribed toolpath originates from two reasons, the accumulation of residual charge [11,15,16], and the prescribed toolpath. The charge-related fiber deviation is mainly represented by the electrostatic interaction between the jet and the preexisting fibers, which has been extensively studied in previous studies [9,17,18]. The toolpath-related fiber deviation, however, has yet to be systematically investigated [19].

For a MEW process, to enable fiber printing without distortion from compressive buckling forces, the translational stage speed v is required to exceed a critical value, namely the critical translational speed (*cts*), whose value equates to the speed of the jet segment at the instant before deposition [20]. Otherwise, the jet will be distorted due to its impact with the collector and coiled into different patterns (sinusoidal curve, '8′

* Correspondence to: 1 Castle Point Hudson, Hoboken, NJ 07030, USA.
E-mail address: rchang6@stevens.edu (R.C. Chang).

https://doi.org/10.1016/j.addma.2022.103035
Received 29 March 2022; Received in revised form 21 June 2022; Accepted 11 July 2022
Available online 14 July 2022
2214-8604/© 2022 Elsevier B.V. All rights reserved.

shaped curve, etc.) [21]. The difference between *v* and *cts* results in the occurrence of jet lag, i.e., the instantaneous contact point of the jet (*cp*) on the collector lags behind the projection point of the nozzle on the collector (i.e., the nozzle position, *np*) [17,22] viewed by a fixed observer on the stage. The magnitude of jet lag can be evaluated by the distance between *np* and *cp*, namely jet lag length (*l*)[23]. The variable *l* is dependent on several process parameters, including the applied voltage, flow rate, and material temperature and is observed o increase as the speed ratio (*v*/*cts*) increases [14]. A consequence of jet lag is the apparent discrepancy between the trajectory of *np* and *cp* relative to the collector, which corresponds to the prescribed toolpath and the pattern of the printed fibers, respectively. For the case of straight fiber printing, this undesired toolpath-related fiber deviation is not perceived because the trajectories of *np* and *cp* relative to the collector are always on the same line regardless of the stability of the jet lag. Therefore, this does not represent a serious consideration for straight fiber printing. Even so, this toolpath-related deviation can be observed when *np* encounters the pin turns along the toolpath. In addition to the common straight fiber printing, another printing mode is curly fiber printing, wherein the target fiber pattern is a general curve (with a nonzero curvature) [13]. This specific mode of printing is of particular relevance to engineered tissues where 3D scaffolds composed of curly fibers are purported to better mimic the natural extracellular matrix [24,25]. For the scenario of curly fiber printing, when the movement of *np* relative to the collector continuously changes in direction, the trajectory of *np* and *cp* relative to the collector don't overlap anymore. In other words, the movement of *np* relative to the collector is unable to be reliably recapitulated by *cp* due to the jet lag [27]. Moreover, when the jet lag length is relatively large or the stage movement abruptly changes in direction, the discrepancy between *np* and *cp* trajectory can be quite significant, resulting in adverse printing outcomes. Xu et al. firstly introduced circular arc toolpath to expand the scaffold complexity and found that a match between the jet speed and the stage speed helps to alleviate this problem. Hrynevich et al. firstly attempted to address this problem for a randomly curly toolpath. Based on a geometrical model, the patterns of printed fibers are accurately predicted when the *np* trajectory is in circular, sinusoidal, and square curves [27]. However, the developed algorithm is deficient with respect to systematic mathematical interpretation, which prevents further understanding of the essential relationship of *np* and *cp* movement. Moreover, this geometrical model prediction of the *cp* trajectory relies solely on the known curly *np* trajectory. The converse of this problem wherein the toolpath design in curly fiber printing is well-defined a priori, i.e., the design of *np* trajectory based on the target *cp* trajectory, is yet unresolved and of potentially greater relevance and practical importance. Hochleitner et al. fabricated crimped elastomer scaffold at a below-the-critical stage speed [26]. Liashenko et al. fabricated nonlinear fibers including sinusoidal, dome, circular shapes [13]. Saidy et al. printed scaffold with serpentine architectures to mimic the wavy nature of the collagen fibers and their load-dependent recruitment for heart valve tissue engineering. However, toolpath design for fibers of more complicated or randomly curly shapes have not been attempted yet.

In this study, by way of vector analysis and differential geometry, the position and speed relationship between the *np* and *cp* movement are found to be governed by two equations, termed the position- and speed-matching (denoted as PM and SM) equations, respectively. Based on the equations, the effect of jet lag, *l* and its stability on the toolpath-related deviation is clarified. Moreover, the importance of real-time identification of *cp* and dynamic speed control is highlighted. These reported outcomes serve to analytically understand the toolpath-related fiber deviation, thereby laying the foundation for toolpath design in curly fiber printing.

2. Materials and methods

2.1. Material preparation

Poly(ε-Caprolactone) (PCL) is in the form of pellets with a mean molecular weight of 45,600 g/mol, mass density of 1.021 g/mL, and polydispersity of 1.219 (Capa 6500, Perstop Ltd. Of UK). A 5 mL pneumatic syringe (Intellispence, Agoura Hills, CA, USA) is loaded with PCL pellets and placed in the heating oven (90 ℃) overnight with its needle-end upside. After each experiment, the syringe is kept at room temperature to avoid unnecessary thermal degradation.

2.2. MEW system configuration

The MEW system used in this study is schematized in Fig. 1. The pneumatic syringe loaded with PCL pellets is heated by a double-walled heating vessel made from alumina ceramics. Between the outer and inner walls of the heating vessels is a heating pad (New Era Pump Systems, Farmingdale, NY, USA) set at 90 ℃. The syringe is connected to an air dispenser (Intellispense, Agoura Hills, CA, USA), which can regulate its output air pressure. The nozzle of the syringe is connected to the positive terminal of a high voltage supply (Stanford Research Systems, Sunnyvale, CA, USA), while the grounded negative terminal is connected to the collector plate. The collector plate (203 mm × 203 mm×3.3 mm, shown in Fig. 1) is fixed on an XY moving platform consisting of two slides (Velmex, USA) driven by step motors. The ambient temperature is kept at 23.5 ± 1 ℃. The key parameters enabling the MEW process are listed in Table 1.

2.3. Imaging and data measurement

A 1080 P, 60FPS, industry microscope camera with 0.5 × to 4.5 × objective (Lapsun, CN) is positioned suitably to track the jet lag during the printing process as shown in Fig. 1. The method of jet lag tracking can be found in detail in previous studies [28]. All the temperatures are measured with a thermometer (Traceable 4039, USA). For all the data, three sampling points are measured, and the mean of them is taken as the result. The standard deviations of the data are shown by the error bars.

2.4. Error analysis

As shown in Fig. 2, to evaluate the printing accuracy, the printed curly fiber is imaged and its profile is detected to get a curve represented by $\vec{r}^{cp,\ ac}$ (red curve in Fig. 2). The target *cp* trajectory is represented by $\vec{r}^{cp}$ (green curve in Fig. 2). These two curves are translated and

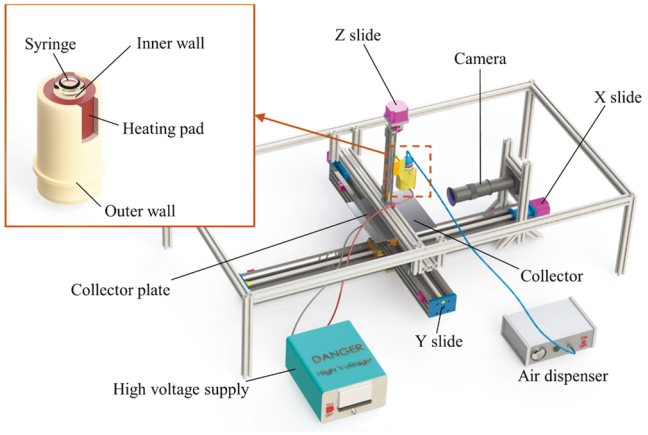

Fig. 1. Schematic of the MEW system, reproduced and adapted with permission from the reference [15].

Table 1
The parameters and their values or range in the MEW process.

Parameters	Values
Heating pad set temperature	90 °C
Voltage (U)	13.5–15.5 kV
Pressure (P)	10 psi
Tip-to-collector distance (D)	15 mm
Translational stage speed (v)	10 mm/s

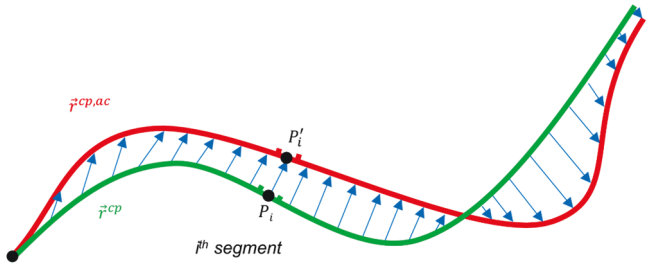

Fig. 2. Evaluation of printing error, or the difference between of $\vec{r}^{cp}$ and $\vec{r}^{cp,\ ac}$.

oriented so that their starting points and initial orientations coincide. Moreover, these two curves are divided into N segments of equal lengths. The curve length of the ith segment is denoted as Δs_i^{cp}. P_i and P_i' are arbitrarily selected points on the ith segment of $\vec{r}^{cp}$ and $\vec{r}^{cp,\ ac}$ curves, respectively. In this way, the printing error can be defined in Eq. (1).

$$Error := \frac{1}{\bar{d}_f} \lim_{N\to N_{\max}} \frac{\sum_{i=1}^{N} \left|\overrightarrow{P_i P_i'}\right| \Delta s_i^{cp}}{\sum_{i=1}^{N} \Delta s_i^{cp}} = \frac{1}{\bar{d}_f} \lim_{N\to N_{\max}} \frac{\sum_{i=1}^{N} \left|\overrightarrow{P_i P_i'}\right|}{N} \approx \frac{1}{\bar{d}_f} \frac{\int_0^{\mathscr{S}^{cp}} |\vec{r}^{cp,\ ac} - \vec{r}^{cp}| ds^{cp}}{\mathscr{S}^{cp}} \tag{1}$$

$\bar{d}_f$ denotes the mean fiber diameter. $\mathscr{S}^{cp}$ denotes the total curve length of the target cp trajectory. N_{max} is the maximum possible value for N to ensure the smoothness of $\vec{r}^{cp,\ ac}$ curve, which is determined by the resolution of the sample image.

3. General model formulation

3.1. Absolute and relative movement in MEW

An MEW process can be implemented either by moving the collector plate while immobilizing the nozzle or by moving the nozzle while immobilizing the collector [29]. In either case, the pattern of the deposited fiber is essentially the trajectory of the contact point, cp, relative to the collector as shown in Fig. 3a. Moreover, the designed toolpath is essentially the trajectory of the nozzle position, np, relative to the collector. Based on this consideration, it is crucial to notice that the

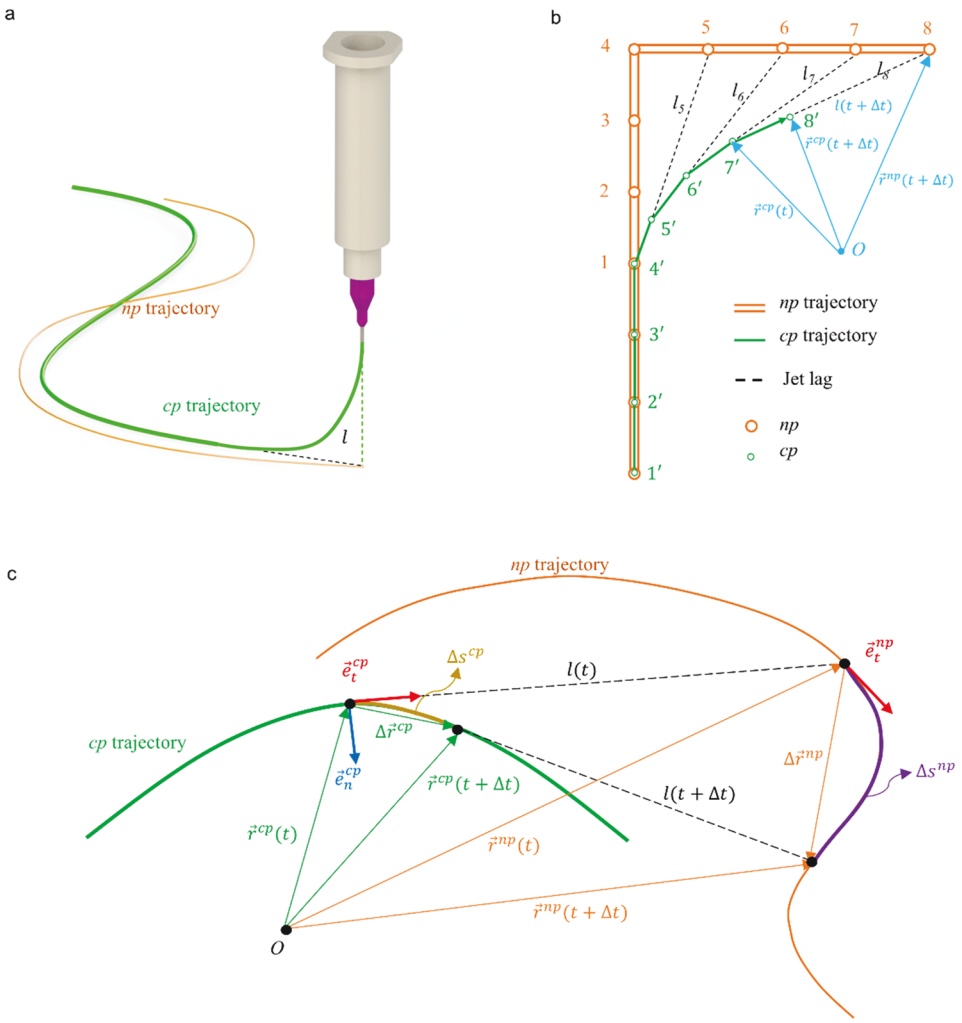

Fig. 3. Relationship between np (orange curve) and cp (green curve) trajectory. (a) The schematic of np, cp trajectory and jet lag. The arrows in blue denote the relationship between $\vec{r}^{np}(t+\Delta t)$, $\vec{r}^{cp}(t+\Delta t)$, $\vec{r}^{cp}(t)$, and $l(t+\Delta t)$. O is an arbitrarily selected origin. (c) The topview of np, cp trajectory with jet lag in general curly fiber printing. The superscripts np and cp denote the nozzle position and contact point, respectively. $\vec{r}$ denotes radius vector. $\vec{e}_t$(red arrows) and $\vec{e}_n$(blue arrow) denote the unit tangential and normal vector. l denotes the jet lag length. s denotes the arc length parameter. (For interpretation of the references to colour in this figure legend, the reader is referred to the web version of this article.)
(b) The topview of np, cp trajectory, and jet lag for a right turn in the np trajectory, reproduced and adapted with permission from References [27].

physical quantities (velocity, speed, radius vector, etc.) symbolized by lowercase letters herein are defined with respect to a coordinates system (*xyz*) attached to the stage and therefore are considered relative quantities. In other words, all these relative physical quantities symbolized by lowercase letters are observed from an observer fixed on the collector plate and thus can't perceive the movement of the stage. If the applied MEW setup includes a movable nozzle and a stationary collector plate, then there will be no difference between the relative and absolute quantities [30].

3.2. Position relationship between *np* and *cp*

In the geometrical model proposed by Hrynevich et al.[27], the patterns of the printed fibers can be accurately predicted so as to verify the model accuracy. Based on the principles inherent to this geometrical model as shown in Fig. 3b, it is reasonable to extract the assumption that the contact point at the next time instant, $cp(t+\Delta t)$ (e.g., Point 8′ in Fig. 3b) is collinear with the current contact point, $cp(t)$ (e.g., Point 7′ in Fig. 3b) and the nozzle position at the next time instant, $np(t+\Delta t)$ (e.g., Point 8 in Fig. 3b) for any current time instant *t*. As shown by the blue arrows in Fig. 3b, this relationship can be expressed in a vectorized equation as follows:

$$\vec{r}^{np}(t+\Delta t)-\vec{r}^{cp}(t+\Delta t)=l(t+\Delta t)\frac{\vec{r}^{cp}(t+\Delta t)-\vec{r}^{cp}(t)}{\left|\vec{r}^{cp}(t+\Delta t)-\vec{r}^{cp}(t)\right|} \tag{2}$$

When $\Delta t\to 0$, $\vec{r}^{cp}(t+\Delta t)-\vec{r}^{cp}(t)\to d\vec{r}^{cp}$ and $\left|\vec{r}^{cp}(t+\Delta t)-\vec{r}^{cp}(t)\right|\to\left|d\vec{r}^{cp}\right|=ds^{cp}$. $\vec{r}^{np}$ and $\vec{r}^{cp}$ are the radius vectors of *np* and *cp*, respectively. Furthermore, s^{cp} is the arc length parameter of the *cp* trajectory as shown in Fig. 3c and *l* is the instantaneous jet lag length. If the unit tangential vector of the *cp* trajectory is denoted as $\vec{e}_t^{cp}$, then $\vec{e}_t^{cp}=\frac{d\vec{r}^{cp}}{ds^{cp}}$. Therefore, Eq. (3) can be derived as follows:

$$\vec{r}^{np}=\vec{r}^{cp}+l\vec{e}_t^{cp} \tag{3}$$

The geometrical significance of Eq. (3) has been shown in Fig. 3c.

Eq. (3) dictates the general positional relationship between *np* and *cp*, regardless of the *cp* trajectory and jet lag stability, and thus can be named the general position-matching (PM) equation. From the general PM, it is important to notice that when $\vec{r}^{cp}$ is predefined, $\vec{e}_t^{cp}$ can be known for any point on the *cp* trajectory. If the dynamic jet lag length *l* is determined for the same point as well, $\vec{r}^{np}$ can be calculated.

3.3. Speed relationship between *np* and *cp*

The general PM defines only the position information of *np* with respect to *cp*, which is not sufficient to define a complete toolpath. What's additionally required is the speed information of *np*, i.e., v^{np}. Since *np* and *cp* continuously move relative to the collector while obeying Eq. (3), there must exist a definite speed relationship between their movement as schematized in Fig. 3c. When the target fiber pattern is known, most of the quantities, including $\vec{r}^{cp}$ and $\vec{e}_t^{cp}$, on the right-hand side of Eq. (3) can be determined when the arc length parameter of *cp* trajectory s^{cp} is specified (corresponding to any specific point on the *cp* trajectory). Therefore, these quantities can be called path variables since they can be determined prior to the printing process. An exception is the jet lag length *l*, which cannot be determined simply from the value of s^{cp} prior to the printing process.

If a specific printing process is considered, there is a one-to-one correspondence between the time instant *t* and s^{cp}. Therefore, s^{cp} can be regarded as a function of *t* or vice versa (i.e., $s^{cp}(t)$ or $t(s^{cp})$). Accordingly, all the quantities in Eq. (3) can be treated as variables depending solely on *t* or s^{cp}. Therefore, it is mathematically permissible to take the derivative with respect to either *t* or s^{cp} for all the terms in Eq. (3). Herein *t* is selected for derivation as shown in Eq. (4), but the same result can be obtained when s^{cp} is selected for derivation as shown in Support Information (Support Part I).

$$\vec{v}^{np}=\vec{v}^{cp}+\dot{l}\vec{e}_t^{cp}+l\frac{d\vec{e}_t^{cp}}{dt} \tag{4}$$

Considering the chain rule and Frenet-Serret formulas[31], it follows that $\frac{d\vec{e}_t^{cp}}{dt}=\frac{ds^{cp}}{dt}\frac{d\vec{e}_t^{cp}}{ds^{cp}}=v^{cp}\kappa^{cp}\vec{e}_n^{cp}$, where κ^{cp} is the local curvature of the *cp* trajectory. This can be substituted into Eq. (4) to get Eq. (5) as follows.

$$\vec{v}^{np}=\vec{v}^{cp}+\dot{l}\vec{e}_t^{cp}+v^{cp}l\kappa^{cp}\vec{e}_n^{cp} \tag{5}$$

The physical significance of Eq. (5) can be interpreted as follows. The difference between the *np* and *cp* velocity includes two terms $\dot{l}\vec{e}_t^{cp}$ and $v^{cp}l\kappa^{cp}\vec{e}_n^{cp}$, which are attributed to the jet lag instability and directional change in *cp* trajectory, respectively.

Based on the definition of velocity, $\vec{v}^{cp}=\frac{d\vec{r}^{cp}}{dt}=\frac{ds^{cp}}{dt}\frac{d\vec{r}^{cp}}{ds^{cp}}=v^{cp}\vec{e}_t^{cp}$ and likewise, $\vec{v}^{np}=v^{np}\vec{e}_t^{np}$. Substituting them into Eq. (5), Eq. (6) can be derived.

$$v^{np}\vec{e}_t^{np}=\left(v^{cp}+\dot{l}\right)\vec{e}_t^{cp}+v^{cp}l\kappa^{cp}\vec{e}_n^{cp} \tag{6}$$

Since $\vec{e}_t^{cp}$ is orthogonal to $\vec{e}_n^{cp}$, Eq. (6) can be considered as the decomposition of the vector $v^{np}\vec{e}_t^{np}$ along two orthogonal directions oriented by $\vec{e}_t^{cp}$ and $\vec{e}_n^{cp}$, with the corresponding components being $v^{cp}+\dot{l}$ and $v^{cp}l\kappa^{cp}$, respectively. Calculating the magnitude of the vectors on both sides of Eq. (6), Eq. (7) can be derived.

$$v^{np}=\sqrt{\left(v^{cp}+\dot{l}\right)^2+\left(v^{cp}l\kappa^{cp}\right)^2} \tag{7}$$

With no additional conditions imposed, Eq. (7) dictates the speed relationship between *np* and *cp* and is a corollary to the general PM. Therefore, it can be named the general speed-matching (SM) equation.

4. Results and discussion

The aforementioned model can be generally applied, regardless of the shape of *cp* trajectory and jet lag stability. However, a real-time measurement of v^{cp} is technically problematic for a curly *cp* trajectory as explained later. Therefore, the representations of the general PM and SM in two special cases, namely the straight fiber printing, and the steady curly fiber printing, are discussed herein.

4.1. Special case 1: straight fiber printing

For a straight fiber printing process, $\kappa^{cp}\equiv 0$, $\vec{e}_t^{np}=\vec{e}_t^{cp}$. Therefore, Eq. (6) can be reduced to Eq. (8).

$$v^{np}=v^{cp}+\dot{l} \tag{8}$$

For a steady straight fiber printing process, $v^{np}=v^{cp}$, therefore, $\dot{l}=0$. In other words, a steady straight fiber printing process is always accompanied by a stable jet lag. Therefore, the reduced form of the general SM in this case is consistent with the definition of steady straight fiber printing process.

In the straight fiber printing process, it is interesting to think about how the jet will react to an instantaneous change in v^{np}. Since it takes time to transfer the change in motion from the nozzle to the *cp*, as v^{np} is instantaneously increased to a higher value (as shown in Fig. 4a), v^{cp} is not affected immediately. In this case, along with Eq. (8), $\dot{l}>0$, implying that the jet is exposed to a stronger stretching force from the collector. This, in turn, results in a higher jet deposition rate and v^{cp} starts to increase. As the difference between v^{np} and v^{cp} becomes less significant, the stretching force applied on the jet becomes weaker, and the increasing rate of v^{cp} will decrease. Finally, when v^{cp} increases to be equivalent to v^{np}, a new stable state is reached. During the transition

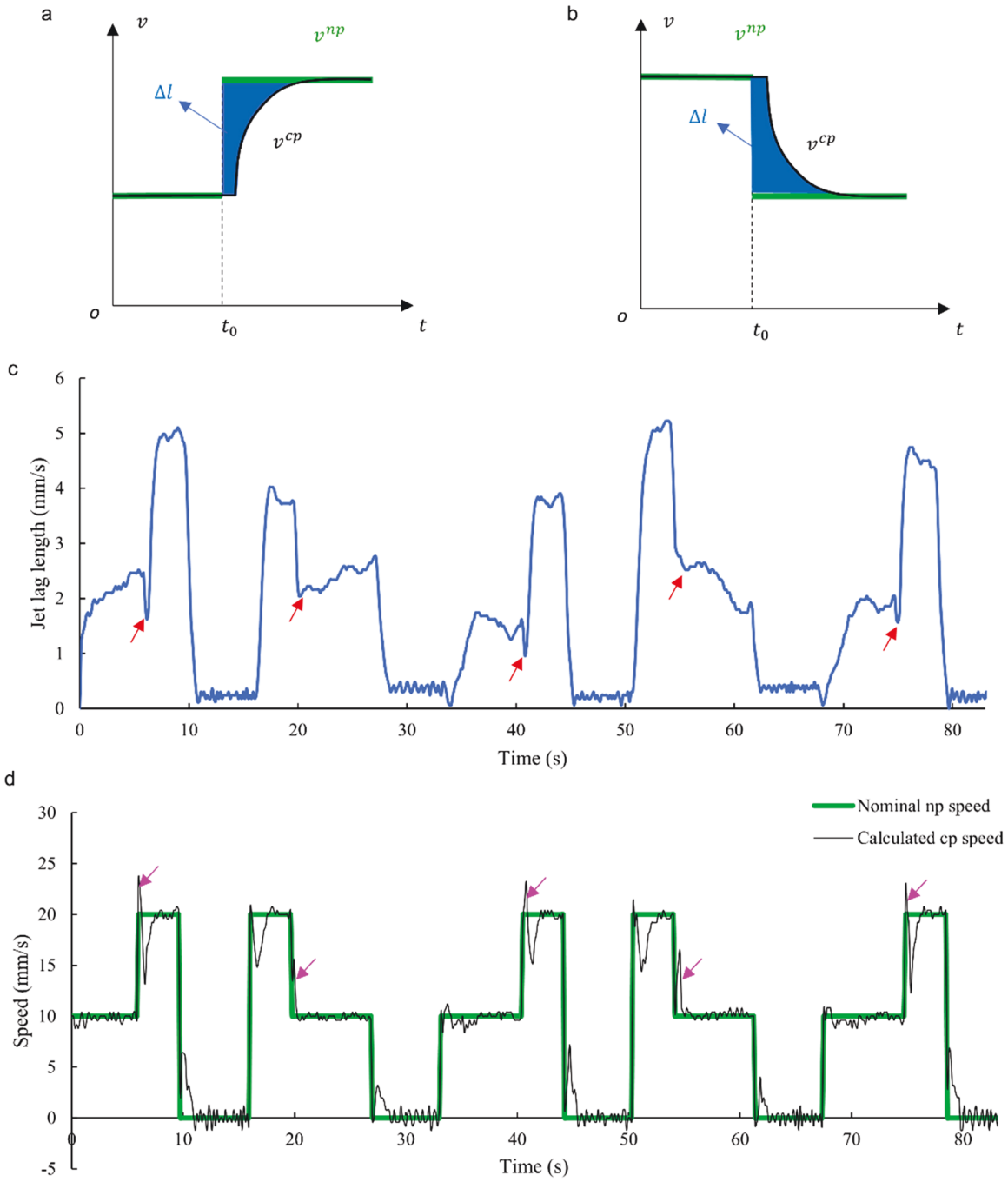

Fig. 4. Evolution of v^{cp} when the stage instantaneously accelerates or decelerates. (a) and (b) are the schematic evolution of v^{cp} predicted by Eq. (8). The green line denotes v^{np} and the black curve denotes v^{cp}. The blue shaded area denotes the change in jet lag length during the transition process. It is assumed that the system is initially in a steady state and eventually arrive a new steady state after the change in v^{np}. (c) shows the jet lag length evolution when the stage instantaneously accelerates or decelerates. When the stage speed switches between 10 mm/s and 20 mm/s (as shown by the green curve in (d)), a trough will arise on the jet lag length signal due to the temporary pauses of the stage, which are attributed to a delayed communication between the motor and the controller. The corresponding nominal (i.e., set) v^{np} evolution as well as the calculated v^{cp} evolution has been shown in (d). The v^{cp} evolution is calculated (black curve in (d)) based on Eq. (8), jet lag evolution and the nominal v^{np} evolution. Due to the abovementioned troughs in the jet lag length signal, a peak will arise on the calculated v^{cp} curve denoted by a magenta arrow in (d). (For interpretation of the references to colour in this figure legend, the reader is referred to the web version of this article.)

process, the jet lag length is increased by Δl (shaded in blue in Fig. 4a). A similar rationale can be made for the case when v^{np} is instantaneously decreased (shown in Fig. 4b).

However, the actual instantaneous reaction of the jet to the v^{np} change is complicated by the mechanical limitation of the stage. As shown in Fig. 4c and d, the jet lag length is tracked when v^{np} is switched between 10 mm/s and 20 mm/s (green curve in Fig. 4d). Based on Eq. (8), the nominal v^{np} (i.e. the set value), and the jet lag length evolution in Fig. 4c, v^{cp} is calculated as shown by the black curve in Fig. 4d (i.e., calculated v^{cp} = nominal $v^{np} - \dot{l}$). From Fig. 4c, when v^{np} transitions from one value to another, there is a temporary pause of the stage due to the delayed communication between the motor and the controller. Around the pause point, the stage will experience a deceleration succeeded by an acceleration process. Therefore, there will arise a trough (denoted by red arrows in Fig. 4c) on the jet lag length signal around the

pause point. Accordingly, there will arise a peak (denoted by magenta arrows in Fig. 4d) on the calculated v^{cp} curve. If these peaks are neglected, the v^{cp} curve will be similar to those in Fig. 4a and b.

4.2. Special case 2: steady curly fiber printing

Before proceeding with the discussion on curly fiber printing, it is necessary to give an appropriate definition of steady curly fiber printing. Herein the time derivative of jet lag length, $\dot{l}$ is selected as the indicator of stability in curly fiber printing (i.e., $\dot{l} = 0$ means steady curly fiber printing) for two reasons. First, all the quantities except l on the right-handed side of Eq. (3) are path variables. If l is additionally kept constant, $\overrightarrow{r}^{np}$ can be determined prior to the printing process, which facilitates the toolpath design a priori. Second, since a steady straight fiber printing is always accompanied by a stable jet lag length according to Eq. (8), it is natural to extend this relationship to the steady curly fiber printing for consistency.

When $l = l_0$, the general PM and SM, i.e., Eq. (3) and Eq. (7), are reduced to the steady PM and SM equations i.e., Eq. (9) and Eq. (10), respectively.

$$\overrightarrow{r}^{np} = \overrightarrow{r}^{cp} + l_0 \overrightarrow{e}_t^{cp} \tag{9}$$

$$\frac{v^{np}}{v^{cp}} = \sqrt{1 + (l_0 \kappa^{cp})^2} \tag{10}$$

Now it is important to notice that when v^{np} is tuned according to v^{cp} as denoted by Eq. (10), a constant l_0 can be maintained throughout the printing process (as schematized in Fig. 3c when l is replaced by l_0). In this way, a steady curly fiber printing can be enabled.

Based on the steady SM, for a steady curly fiber printing process, v^{np} is affected not only by v^{cp}, but also by the jet lag length l_0 and the curvature of the *cp* trajectory, κ^{cp}. Since v^{np} cannot increase without bound considering the mechanical limitations of the stage, to avoid a v^{np} beyond these mechanical bounds, l_0 cannot be set at an arbitrarily high value (by tuning the process parameters, e.g., voltage, material temperature, etc.). This implies that a match between the jet speed and v^{np}, which result in a reasonable jet lag length, is important to improve the printing accuracy, as indicated by other studies [32]. By the same token, a dramatic directional change in the *cp* trajectory should be avoided. Moreover, it is theoretically unlikely to print a *cp* trajectory with a sharp turn ($\kappa^{cp} \to \infty$), because l_0 can't be zero [27], which yields an infinitely large $l_0 \kappa^{cp}$ and v^{np} in this case.

To experimentally verify the steady PM and SM, some additional details are warranted. First, to avoid a complicated measurement of κ^{cp}, a circular *cp* trajectory (i.e., κ^{cp} is constant) is adopted herein. Second, based on the steady PM and the circular *cp* trajectory, the *np* trajectory should be a larger concentric circle as shown in Fig. 5a. Therefore, if a *np* trajectory like the yellow circle is applied and a *cp* trajectory like the black circle is observed, the steady PM can be verified. Last, to verify the steady SM, it is necessary to find the special form of the steady SM in this case. Since the *cp* trajectory is a circle, $\kappa^{cp} \equiv \frac{1}{r^{cp}}$. Based on the steady SM, $\frac{v^{np}}{v^{cp}}$ remains constant throughout the process. In addition, since a steady

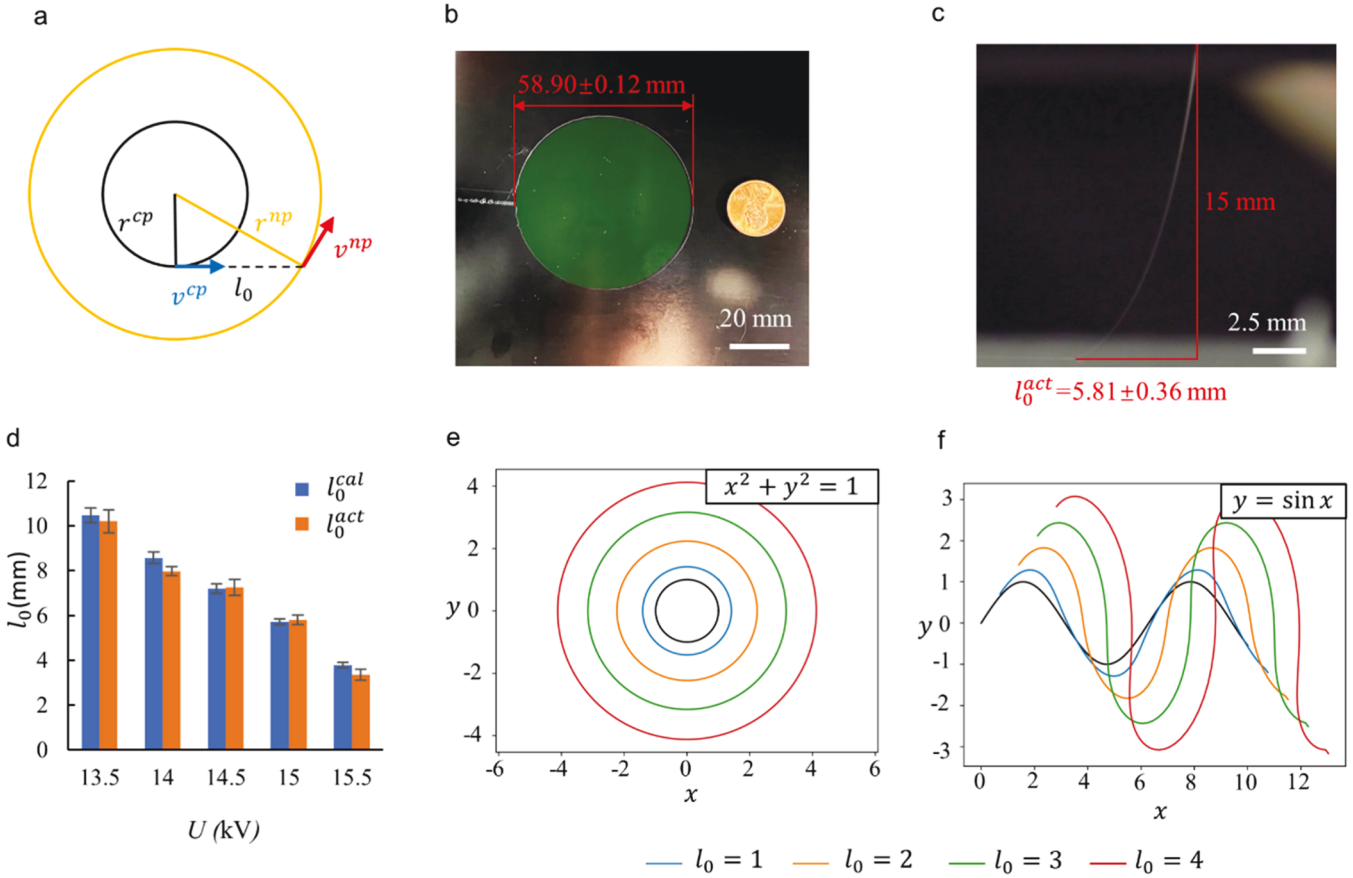

Fig. 5. Determination of *np* trajectory for stable curly fiber printing. (a) schematizes the relationship between r^{np}, r^{cp}, and l_0 for a circular *cp* trajectory. (b) shows the printed fiber pattern with a diameter of 58.90 ± 0.12 mm. The green area is a perfect circle. The *np* trajectory is a circle with a radius of 30 mm. (c) shows the jet lag for printing the fiber pattern in (b). The distance between the nozzle and the collector is 15 mm, and the actual jet lag length l_0^{act} is 5.81 mm. (d) show the comparison of the calculated jet lag length l_0^{cal} and l_0^{act} when the voltage U varies, and the *np* trajectory is a circle with a radius of 30 mm. (e) and (f) show the predicted effect of the jet lag length on the *np* trajectory for a circular and sinusoidal *cp* trajectory, respectively based on the steady PM. The black curves denote the *cp* trajectories, while the colorful curves denote the *np* trajectories at different jet lag lengths.

printing process also means that the speed is proportional to curve length, then it follows that $\frac{v^{np}}{v^{cp}} = \frac{2\pi r^{np}}{2\pi r^{cp}} = \frac{r^{np}}{r^{cp}}$. Substituting this and $\kappa^{cp} = \frac{1}{r^{cp}}$ into Eq. (10), Eq. (11) can be derived.

$$r^{np2} = r^{cp2} + {l_0}^2 \tag{11}$$

r^{np} and r^{cp} are the magnitude of radius vector of *np* and *cp* trajectory when the origin of the circle is selected as the origin. Therefore, r^{np}, r^{cp}, and l_0 can be regarded as the side lengths in a right triangle as shown in Fig. 5a. Eq. (11) can be regarded as the special form of the steady SM in this case. Therefore, if r^{np}, r^{cp}, and l_0 are found to follow Eq. (11), the steady SM can be verified.

As is shown in Fig. 5b, when a circular toolpath (r^{np}=30 mm) is adopted, the good circularity of the printed fiber pattern (compared to a perfect circle denoted by the green shaded area) is consistent with the prediction, thus verifying the steady PM. Based on the methodology described in Section 2.4, the Error between the printed fiber pattern and the predicted *cp* trajectory (calculated from *np* trajectory and l_0^{act}, as shown in as shown in Fig. S1) is 3.05. The mean diameter of printed fiber pattern is approximately 58.9 mm, which means r^{cp}= 29.45 mm. Based on Eq. (11), the calculated jet lag length l_0^{cal}= 5.72 mm. By tracking the jet lag, the actual jet lag length l_0^{act}= 5.81 mm (Fig. 5c), which is consistent with the predicted value, thus verifying the steady SM. For further verification, when the voltage varies from 13.5 kV to 15.5 kV, different jet lag lengths can be observed, l_0^{act} and l_0^{cal} have been compared in Fig. 5d.

Based on the steady PM, the *np* trajectory can be predetermined for a constant jet lag length l_0. An interesting question herein is to theoretically predict the effect of l_0 on the *np* trajectory. As shown in Fig. 5e and f, different l_0 are selected when the *cp* trajectory is a circular or sinusoidal curve, respectively. It can be shown that the larger the jet lag length is, the more significant the difference is between *cp* and *np* trajectory.

5. Limitations

It should be noted that all of the derivations are developed based on Hrynevich's geometrical model [27] without introducing additional conditions and physical assumptions. Therefore, it can be regarded as a mathematical interpretation of it, whose accuracy has been largely verified considering its enhanced performance in predicting the printed fiber pattern [27]. Moreover, the reduced forms of the model are well consistent with the experimental results in straight fiber printing and steady curly fiber printing. However, several limitations need to be considered for its applicability.

First, to ensure a jet's projection tangential to the *cp* trajectory, the collector needs to be smooth and the residual charge in the preexisting fiber is insignificant [15] so that the local electric field is not affected. Since the ultimate objective of this model formulation is to implement the curly fiber printing, these requirements need to be met by the operator by way of careful selections of the collector and alleviation for residual charge accumulation. Second, the model is developed mainly based on geometrical considerations with little consideration for the physics of MEW and the material properties (i.e., rheological properties). However, this never means that other process parameters and material properties have no effects on the printing accuracy in curly fiber printing. Instead, their collective effects are expected to be reflected in the change of v^{cp}, which can be real-time measured in the implementation of curly fiber printing. Last, based on the proposed model, the implementation of curly fiber printing faces two challenges. On one side, the movement of most current translational stages cannot execute a smooth curly toolpath. Instead, the curly toolpath has to be segmented and each segment is approximated by a line (i.e., piecewise linear interpolation) based on the mechanical limitations of the stage. The performance of approximation improves when the density of segments increases. However, when the length of each segment is too small, the actual stage speed will be inaccurate due to the delayed communication between the controller and motors (as shown in Fig. 4c). On the other hand, the calculation of v^{np}requires v^{cp} or a real-time identification of *cp*, which is another challenge. The conventional image-based *cp* identification needs to be improved by utilizing autofocusing cameras (as shown in Fig. S2) because *cp* will be blurry when it deviates from the focal plane of the camera, which usually happens in curly fiber printing. More *cp* identification methodologies await development of advanced collector surface materials that serve as thermoelectric and piezoelectric sensors to track the deposited fibers on the collector (as shown in Fig. S3).

6. Conclusions

In this study, the position and speed relationships between *np* and *cp* are found by means of vector analysis and differential geometry, which follow position- and speed-matching equations (PM and SM), respectively. Moreover, these relationships in two special cases, namely straight fiber printing and steady curly fiber printing, are also given and verified. For the circular and sinusoidal *cp* trajectory in steady curly fiber printing, the effects of jet lag length l_0 on the *np* trajectory are investigated. Moreover, the printing accuracy is evaluated by the Error, an indicator to characterize the difference between the target *cp* trajectory and the actual *cp* trajectory.

In this investigation, the formulation of PM and SM equations lay the theoretical foundation for the curly fiber printing. The PM and SM equations provide the necessary information to design a complete toolpath for curly fiber printing. However, successful implementation of curly fiber printing still requires development of translational stages with more sophisticated control and a facile way to identify *cp* in a real-time manner. The dynamic control of v^{np} based on v^{cp} for MEW process is an important and promising future direction in curly fiber printing, whose basic principle has been shown in the Supporting Information (Support Part II). Moreover, it should be noted that the curly fiber printing introduced herein reflects only the toolpath-related fiber deviation. The charge-related fiber deviation, however, is not considered. Due to the autofocusing effect caused by charge polarization, the pattern of printed fibers on subsequent layers are expected to follow the same trajectory when the charge effect is not significant. More investigations are required to maintain the printing accuracy when large-volume curly-fiber structures are printed.

Funding

The research was funded by the National Science Foundation under Award No. CMMI-MME-1663095 and the U.S. Army Medical Research Acquisition Activity under Award No. USMRAA-W81XWH-19–1–0158. Any opinions, findings, and conclusions or recommendations expressed in this publication are those of the authors and do not necessarily reflect the views of the National Science Foundation or the U.S. Army Medical Research Acquisition Activity.

CRediT authorship contribution statement

Kai Cao: Conceptualization, Data curation, Formal analysis, Investigation, Methodology, Software, Validation, Visualization, Writing – original draft, Writing – review & editing **Fucheng Zhang:** Conceptualization, Formal analysis, Methodology, Writing – review & editing **Bijun Wang:** Formal analysis, Investigation, Software, Writing – review & editing **Yuning Sun:** Formal analysis, Investigation, Software **Ahmadreza Zaeri:** Investigation, Methodology, Writing – review & editing **Ralf Zgeib:** Methodology, Writing – review & editing **Mo Monsouri:** Supervision, Writing – review & editing **Robert C. Chang:** Conceptualization, Funding acquisition, Project administration, Resources, Supervision, Writing – review & editing.

Declaration of Competing Interest

The authors declare that they have no known competing financial interests or personal relationships that could have appeared to influence the work reported in this paper.

Data availability

Data will be made available on request.

Appendix A. Supporting information

Supplementary data associated with this article can be found in the online version at doi:10.1016/j.addma.2022.103035.

References

[1] M. Castilho, A. van Mil, M. Maher, C.H.G. Metz, G. Hochleitner, J. Groll, P. A. Doevendans, K. Ito, J.P.G. Sluijter, J. Malda, Melt electrowriting allows tailored microstructural and mechanical design of scaffolds to advance functional human myocardial tissue formation, Adv. Funct. Mater. 28 (2018) 1–10, https://doi.org/10.1002/adfm.201803151.

[2] A. Hrynevich, S. Bilge, J.N. Haigh, R. Mcmaster, A. Youssef, C. Blum, T. Blunk, G. Hochleitner, J. Groll, P.D. Dalton, Dimension-based design of melt electrowritten scaffolds, Small 14 (2018), 1800232, https://doi.org/10.1002/smll.201800232.

[3] M. Gwiazda, S. Kumar, W. Świeszkowski, S. Ivanovski, C. Vaquette, The effect of melt electrospun writing fiber orientation onto cellular organization and mechanical properties for application in Anterior Cruciate Ligament tissue engineering, J. Mech. Behav. Biomed. Mater. 104 (2020), https://doi.org/10.1016/j.jmbbm.2020.103631.

[4] T.D. Brown, P.D. Dalton, D.W. Hutmacher, Melt electrospinning today: an opportune time for an emerging polymer process, Prog. Polym. Sci. 56 (2016) 116–166, https://doi.org/10.1016/j.progpolymsci.2016.01.001.

[5] F. Tourlomousis, A. Babakhanov, H. Ding, R.C. Chang, A. Novel Melt Electrospinning System, For studying cell substrate interactions, Int. Manuf. Sci. Eng. Conf. (2015) 1–11, https://doi.org/10.1115/MSEC20159443.

[6] J.C. Kade, P.D. Dalton, Polymers for melt electrowriting, Adv. Healthc. Mater. 10 (2021), https://doi.org/10.1002/adhm.202001232.

[7] W.E. King, G.L. Bowlin, Near-field electrospinning and melt electrowriting of biomedical polymers—progress and limitations, Polym. (Basel) 13 (2021) 1097, https://doi.org/10.3390/polym13071097.

[8] F. Tourlomousis, H. Ding, D.M. Kalyon, R.C. Chang, Melt electrospinning writing process guided by a "printability number", J. Manuf. Sci. Eng. 139 (2017), 081004 https://doi.org/10.1115/1.4036348.

[9] K. Cao, F. Zhang, A. Zaeri, R. Zgeib, R.C. Chang, A charge-based mechanistic study into the effect of collector temperature on melt electrohydrodynamic printing outcomes, Adv. Mater. Technol. (2021), 2100251, https://doi.org/10.1002/admt.202100251.

[10] G. Zheng, G. Fu, J. Jiang, X. Wang, W. Li, P. Wang, Melt electrowriting stacked architectures with high aspect ratio, Appl. Phys. A. 127 (2021) 410, https://doi.org/10.1007/s00339-021-04582-x.

[11] F.M. Wunner, M. Wille, T.G. Noonan, O. Bas, P.D. Dalton, E.M. De-juan-pardo, D. W. Hutmacher, Melt electrospinning writing of highly ordered large volume scaffold architectures, Adv. Mater. 30 (2018), 1706570, https://doi.org/10.1002/adma.201706570.

[12] Y. Jin, Q. Gao, C. Xie, G. Li, J. Du, J. Fu, Y. He, Fabrication of heterogeneous scaffolds using melt electrospinning writing: Design and optimization, Mater. Des. 185 (2020), 108274, https://doi.org/10.1016/j.matdes.2019.108274.

[13] I. Liashenko, A. Hrynevich, P.D. Dalton, Designing outside the box: unlocking the geometric freedom of melt electrowriting using microscale layer shifting, Adv. Mater. 32 (2020), 2001874, https://doi.org/10.1002/adma.202001874.

[14] G. Hochleitner, A. Youssef, A. Hrynevich, J.N. Haigh, T. Jungst, J. Groll, P. D. Dalton, Fibre pulsing during melt electrospinning writing, BioNanoMaterials 17 (2016) 159–171, https://doi.org/10.1515/bnm-2015-0022.

[15] K. Cao, F. Zhang, A. Zaeri, R. Zgeib, R.C. Chang, Quantitative investigation into the design and process parametric effects on the fiber-entrapped residual charge for a polymer melt electrohydrodynamic printing process, Macromol. Mater. Eng. (2022), 2100766, https://doi.org/10.1002/mame.202100766.

[16] J. He, G. Hao, Z. Meng, Y. Cao, D. Li, Expanding melt-based electrohydrodynamic printing of highly-ordered microfibrous architectures to cm-height via in situ charge neutralization (n/a), Adv. Mater. Technol. (2021), 2101197, https://doi.org/10.1002/admt.202101197.

[17] K. Cao, F. Zhang, R.C. Chang, A charge-based mechanistic study into the effects of process parameters on fiber accumulating geometry for a melt electrohydrodynamic process, Processes 8 (2020) 1440, https://doi.org/10.3390/pr8111440.

[18] H. Ding, K. Cao, F. Zhang, W. Boettcher, R.C. Chang, A fundamental study of charge effects on melt electrowritten polymer fibers, Mater. Des. 178 (2019), 107857, https://doi.org/10.1016/j.matdes.2019.107857.

[19] J. Kim, E. Bakirci, K.L.O. Neill, A. Hrynevich, P.D. Dalton, Fiber bridging during melt electrowriting of poly (ε -caprolactone) and the influence of fiber diameter and wall height, Macromol. Mater. Eng. (2021), 2000685, https://doi.org/10.1002/mame.202000685.

[20] P.D. Dalton, Melt electrowriting with additive manufacturing principles, Curr. Opin. Biomed. Eng. 2 (2017) 49–57, https://doi.org/10.1016/j.cobme.2017.05.007.

[21] C. Balda, F. Afghah, B. Saner, Y. Mehmet, Y. Menceloglu, M. Culha, B. Koc, Modeling 3D melt electrospinning writing by response surface methodology, Mater. Des. 148 (2018) 87–95, https://doi.org/10.1016/j.matdes.2018.03.053.

[22] P. Mieszczanek, T.M. Robinson, P.D. Dalton, D.W. Hutmacher, Convergence of machine vision and melt electrowriting, Adv. Mater. (2021), 2100519, https://doi.org/10.1002/adma.202100519.

[23] F.M. Wunner, P. Mieszczanek, O. Bas, S. Eggert, J. Maartens, Printomics: the high-throughput analysis of printing parameters applied to melt electrowriting, Biofabrication 11 (2019), 025004, https://doi.org/10.1088/1758-5090/aafc41.

[24] B.D. James, P. Guerin, Z. Iverson, J.B. Allen, Mineralized DNA-collagen complex-based biomaterials for bone tissue engineering, Int. J. Biol. Macromol. 161 (2020) 1127–1139, https://doi.org/10.1016/j.ijbiomac.2020.06.126.

[25] A.P. Kishan, E.M. Cosgriff-Hernandez, Recent advancements in electrospinning design for tissue engineering applications: a review, J. Biomed. Mater. Res. - Part A 105 (2017) 2892–2905, https://doi.org/10.1002/jbm.a.36124.

[26] G. Hochleitner, F. Chen, C. Blum, P.D. Dalton, B. Amsden, J. Groll, Melt electrowriting below the critical translation speed to fabricate crimped elastomer scaffolds with non-linear extension behaviour mimicking that of ligaments and tendons, Acta Biomater. 72 (2018) 110–120, https://doi.org/10.1016/j.actbio.2018.03.023.

[27] A. Hrynevich, I. Liashenko, P.D. Dalton, Accurate prediction of melt electrowritten laydown patterns from simple geometrical considerations, Adv. Mater. Technol. (2020), 2000772, https://doi.org/10.1002/admt.202000772.

[28] K. Cao, F. Zhang, A. Zaeri, R. Zgeib, R.C. Chang, Advancing a real-time image-based jet lag tracking methodology for optimizing print parameters and assessing melt electrowritten fiber quality, Addit. Manuf. 54 (2022), 102764, https://doi.org/10.1016/j.addma.2022.102764.

[29] M.L. Muerza-Cascante, D. Haylock, D.W. Hutmacher, P.D. Dalton, Melt electrospinning and its technologization in tissue engineering, Tissue Eng. Part B Rev. 21 (2015) 187–202, https://doi.org/10.1089/ten.teb.2014.0347.

[30] J.H. Ginsberg, Relative Motion, in: Adv. Eng. Dyn., Cambridge University Press, 1984, pp. 55–118, https://doi.org/10.1017/CBO9780511800214.004.

[31] W. Kühnel, Differential geometry, Am. Math. Soc. (2015). ⟨https://books.google.com/books?id=qNBYCwAAQBAJ⟩.

[32] H. Xu, I. Liashenko, A. Lucchetti, L. Du, Y. Dong, D. Zhao, J. Meng, H. Yamane, P. D. Dalton, Designing with circular arc toolpaths to increase the complexity of melt electrowriting, Adv. Mater. Technol. 2101676 (2022) 1–8, https://doi.org/10.1002/admt.202101676.